ARTICLES
PUBLISHED ONLINE: 6 FEBRUARY 2011 | DOI: 10.1038/NPHOTON.2010.315
nature photonics

Nanolasers grown on silicon

Roger Chen, Thai-Truong D. Tran, Kar Wei Ng, Wai Son Ko, Linus C. Chuang, Forrest G. Sedgwick and Connie Chang-Hasnain*

The integration of optical interconnects with silicon-based electronics can address the growing limitations facing chip-scale data transport as microprocessors become progressively faster. However, until now, material lattice mismatch and incompatible growth temperatures have fundamentally limited monolithic integration of lasers onto silicon substrates. Here, we use a novel growth scheme to overcome this roadblock and directly grow on-chip InGaAs nanopillar lasers, demonstrating the potency of bottom-up nano-optoelectronic integration. Unique helically propagating cavity modes are used to strongly confine light within subwavelength nanopillars despite the low refractive index contrast between InGaAs and silicon. These modes therefore provide an avenue for engineering on-chip nanophotonic devices such as lasers. Nanopillar lasers are as-grown on silicon, offer tiny footprints and scalability, and are thus particularly suited to high-density optoelectronics. They may ultimately form the basis of future monolithic light sources needed to bridge the existing gap between photonic and electronic circuits.

Since the first laser demonstrated that stimulated emission processes in an optical medium can implement a powerful, coherent light source[1], the field of photonics has witnessed an explosion of applications in telecommunications, lighting, displays, medicine and optical physics, among others. The integration of photonic and electronic devices to combine the advantages of both has subsequently attracted great interest. In particular, the integration of optical interconnects onto silicon chips has become critical as a result of ongoing miniaturization of silicon logic elements having created a bottleneck in inter- and intrachip communications[2,3]. Some approaches towards creating on-chip light sources for optical interconnects have focused on engineering silicon and germanium for optical gain[4–6] and stimulated Raman scattering[7–9]. In other research, III–V lasers have been heterogeneously bonded onto silicon substrates[10–12]. However, numerous challenges face these approaches. Wafer bonding has low yield because of a stringent surface flatness requirement down to the atomic scale, and group IV emitters must overcome an indirect bandgap that offers exceedingly inefficient radiation. Monolithic growth of high-performance III–V lasers on silicon therefore remains a 'holy grail' in the search for cost-effective, massively scalable and streamlined fabrication of on-chip light sources.

To date, the fundamental roadblock facing monolithic integration has been a large mismatch of the lattice constants and thermal expansion coefficients of III–V materials and silicon. Laser materials have previously been grown on silicon substrates, but the required high growth temperatures would be detrimental to existing silicon electronic devices[13–16]. To overcome these barriers, we recently demonstrated the growth of single-crystal GaAs nanoneedles on silicon at 400 °C under conditions compatible with complementary metal-oxide-semiconductor (CMOS) technology[17,18]. Based on this template, we have gone on to develop InGaAs/GaAs heterostructure nanopillar lasers that are monolithically integrated onto silicon after a single growth step. Because of their compatibility with silicon technology, nanopillar lasers can potentially take advantage of the capabilities of today's massive silicon infrastructure to facilitate an ongoing paradigm shift in modern computing architecture towards optoelectronic circuitry. We also show a novel helically propagating mode cavity that offers a unique feedback mechanism to enable on-chip laser oscillation. Whereas traditional Fabry–Pérot modes are inhibited by the interface between InGaAs and silicon, helical modes can strongly localize light within nanopillars of even subwavelength dimensions without lossy plasmonic or metal–optic effects. These modes therefore exemplify how novel optical phenomena in nanostructures can be used for future on-chip nanophotonic devices.

Results

Nanopillar growth on silicon. The nanopillar-based laser is schematically depicted in Fig. 1a. Its cross-section reveals inner core–shell layers (see inset for a top view of the laser). The core contains the InGaAs active region, and the GaAs shell provides surface passivation. Most nanopillars have a slight 5° taper between opposite sidewall facets. The height and diameter of the nanopillars scale easily and controllably with growth time, despite the large lattice mismatch. Typical nanopillars have tiny footprints of only ~0.34 μm^2, enabling them to realize high-density silicon-based optoelectronics. Nanopillars display extremely well-faceted geometry, as shown by the scanning electron microscope (SEM) image in Fig. 1b. The top-view SEM image in Fig. 1c shows the hexagonal cross-section of the nanopillar, which results from its unique single-crystal wurtzite structure[19]. As we will show later, the as-grown nanopillar structure provides a natural optical cavity supporting unique resonances that have not been observed before, to the best of our knowledge. Nanopillars do not therefore require additional top-down processing to form on-chip optical cavities. Instead, they provide a viable bottom-up approach towards integrating light sources and resonators onto a silicon chip.

Importantly, nanopillars have several critical advantages for optoelectronic integration onto silicon. They grow at the low temperature of 400 °C, which is drastically lower than typical III–V growth temperatures by 200–300 °C and is compatible with CMOS devices. Heterostructure nanopillar growth occurs spontaneously on a silicon substrate by metal–organic chemical vapour deposition (MOCVD) and is catalyst-free, avoiding the incorporation of metal particles that are poisonous to silicon CMOS devices.

Department of Electrical Engineering and Computer Sciences and Applied Science and Technology Group, University of California at Berkeley, Berkeley, California 94720, USA. *e-mail: cch@eecs.berkeley.edu

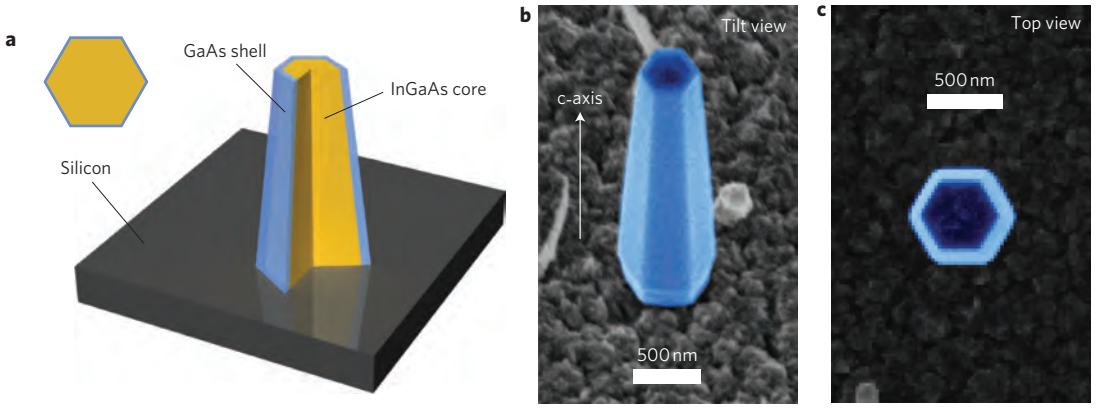

Figure 1 | InGaAs/GaAs heterostructure nanopillar lasers monolithically grown on silicon. a, Schematic of a nanopillar laser monolithically integrated onto silicon, illustrating its InGaAs core and GaAs shell. The higher-bandgap GaAs shell protects carriers from non-radiative surface recombination, which is critical for room-temperature lasing. Inset: top-view schematic. **b**, SEM image showing the well-faceted geometry of the nanopillar optical cavity. This resonator structure forms naturally during growth, allowing lasers to be directly grown on silicon without additional processing. Nanopillar dimensions scale with growth time, enabling the growth of effectively bulk high-quality III–V material on silicon. No critical dimensions have been observed for this novel lattice-mismatched growth mechanism. **c**, Top-view SEM image highlighting the hexagonal wurtzite crystal structure of the nanopillar. This hexagonal symmetry results in whispering gallery-like effects.

Additionally, core–shell layering allows nanopillar laser diode structures to be grown on silicon[20]. (Detailed procedures are described in the Supplementary Information.) Low-temperature and catalyst-free growth allows nanopillars to be monolithically integrated with silicon electronics without compromising highly developed silicon transistor technology and CMOS process flows.

Laser oscillation on silicon. Room-temperature laser oscillation is achieved by optical excitation using a mode-locked Ti:sapphire laser (see Methods). At low pump levels, nanopillars emit broad spontaneous emission. With increasing excitation intensity, a cavity mode emerges, and laser oscillation is ultimately seen at ~950 nm, as shown in Fig. 2a. The inset shows the nanolaser light output power and emission spectral linewidth as functions of excitation (the former is referred to as the 'light–light' or 'L–L curve'). Clear threshold behaviour is observed in the L–L curve, together with prominent clamping of the laser linewidth. A classic signature of lasing is observed from near-field images of nanopillar lasers. When pumped below threshold, a nanopillar only outputs a spot of spontaneous emission, as shown in Fig. 2b. Above threshold, clear speckle patterns due to the interference of highly coherent light become visible (Fig. 2c). Most lasers characterized show single-mode operation, although as many as three lasing modes have been seen from a single nanopillar. We note that growing a sufficiently thick GaAs cap (~90 nm) is key in suppressing surface recombination to enable room-temperature operation. Lasing on silicon at room temperature is a critical achievement, demonstrating the potential of nanopillar lasers for implementing practical optoelectronics beyond the research laboratory.

We performed additional experimental studies at 4 K to further characterize the nanopillar laser and extract various laser parameters. Figure 2d shows the L–L curve and the corresponding spectra below and above lasing threshold for a typical laser: a clear threshold is seen at a very low excitation intensity of ~22 $\mu J\,cm^{-2}$. By constructing an analytical gain model using material parameters from the literature[21], we analysed the spontaneous emission spectrum of the nanopillar and established a correlation between experimental pump levels and carrier density. Applying the gain model with classical rate equation analysis[22,23], we fit the L–L curve in Fig. 2d to reveal a threshold gain and carrier density of ~1,400 cm^{-1} and ~$1 \times 10^{18}\,cm^{-3}$, respectively (see Supplementary Information). We accordingly estimate a cavity quality (Q) factor of ~206 and a spontaneous emission factor of $\beta \approx 0.01$, where β measures the fraction of spontaneous emission coupled into the cavity mode of interest. This value is reasonable considering the laser's small volume of $6 \times 10^{-13}\,cm^3$ (ref. 24). We additionally measured a strong background suppression ratio of ~17–20 dB from typical lasing spectra.

Helically propagating cavity modes. Despite minimal index contrast between the InGaAs nanopillar ($n_r \approx 3.7$) and the silicon substrate it resides on ($n_r \approx 3.6$), sufficient optical feedback or Q is attained for laser oscillation in our novel structures. Even non-negligible absorption by silicon at nanopillar laser wavelengths is overcome. Intuitively, helically propagating modes can have nearly total internal reflection at the nanopillar–silicon interface, because their wave vectors strike that boundary with grazing incidence at extremely shallow angles. Figure 3a illustrates this novel concept using a ray-optics interpretation. Alternatively, the interface between substrate and nanopillar can be thought of as introducing a strong cutoff for helically propagating modes. The strong feedback of helical modes was further confirmed by finite-difference time-domain (FDTD) calculations of untapered nanopillars. These helical nanopillar modes have strong azimuthal components, which result in transverse field profiles similar to those previously reported for hexagonal whispering gallery (WG) modes[25–27], as shown in Fig. 3b. However, unlike traditional WG modes, helical nanopillar resonances have net propagation in the axial direction. This can be seen from the first- and third-order axial standing-wave patterns shown in Fig. 3c and d, respectively.

We can therefore define two mode numbers to describe these helically propagating modes. An azimuthal mode number m describes the transverse field pattern just as it does for WG modes, and an axial mode number n describes the order of the axial standing wave as for Fabry–Pérot resonances. To be complete, a third mode number should account for higher-order radial modes, but we find that the subwavelength transverse dimensions of nanopillars limit access to only the lowest-order radial mode. Both transverse electric (TE) as well as transverse magnetic (TM) polarizations exist. Previous photoluminescence studies indicate that material gain is stronger for an electric field polarized perpendicular to the wurtzite nanopillar axis, suggesting TE modes may be preferred for lasing[28]. In this Article, we refer to specific resonances as either TE_{mn} or TM_{mn} for consistency. As might be expected, modes with distinct mode numbers resonate at distinct wavelengths

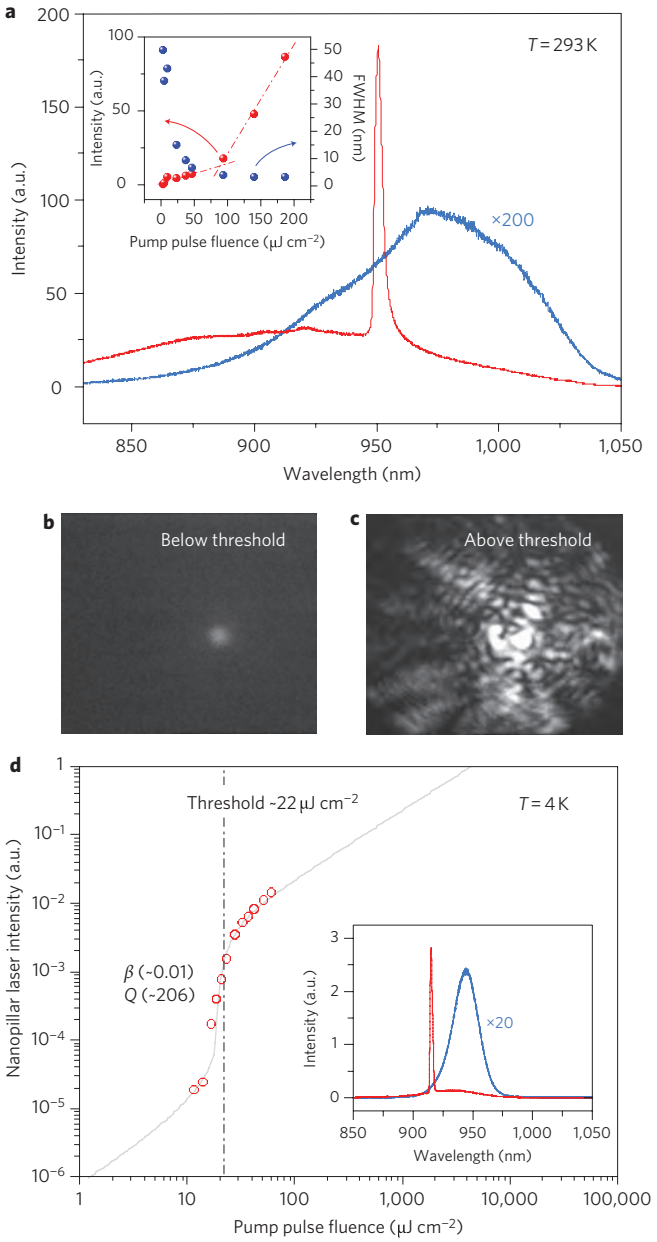

Figure 2 | On-chip nanopillar laser oscillation. a, Room-temperature nanopillar emission below (blue) and above (red) threshold. The spectrum below threshold has been magnified ×200 for visibility. Inset: L–L curve and linewidth clamping of the laser, revealing a threshold at ~93 μJ cm^{-2}. **b**, Camera images of nanopillar emission below threshold show only a spot of spontaneous emission. **c**, Upon lasing, strong speckle patterns appear. Speckle results from the high degree of coherent emission and is a classic signature of laser oscillation. **d**, L–L curve of a nanopillar laser operating at 4 K with a low threshold of ~22 μJ cm^{-2} is analysed to extract estimated values of Q (~206) and β (~0.01). Inset: spectra of the nanopillar laser below (blue, magnified ×20) and above (red) threshold. The laser peak clearly dominates above threshold, achieving a 17 dB background suppression ratio.

(for example, $\lambda_1 = 921$ nm for TM_{61} and $\lambda_3 = 916$ nm for TM_{63}). Both nanopillar radius and length determine cavity resonances, further substantiating the helical nature of nanopillar cavity modes. Meanwhile, traditional WG resonances are relatively insensitive to axial dimension. In our description, they can actually be interpreted as the $n = 1$ subset of helically propagating modes. We find that most nanopillars lase between 890 and 930 nm when the nanopillar radius is varied between 270 and 340 nm. This range corresponds to TM_{5n}, TM_{6n}, TE_{4n} and TE_{5n} resonances, which are among the lowest-order azimuthal modes reported to have achieved laser oscillation. Additional discussion and details of FDTD calculations and results are presented in the Supplementary Information.

The most important consequence of a helically propagating mode is that it allows high reflectivity at a dielectric interface with low index contrast. From Fig. 3c and d, it is evident that the cavity modes are remarkably well confined in the active material, despite the significant interface with silicon. Such strong confinement enables our resonators to lase without having to fabricate the pedestals that WG microdisk lasers typically require to preserve vertical optical confinement. In fact, the confinement is strong enough that even nanopillars with subwavelength dimensions on all sides achieve laser oscillation. An SEM image of such a subwavelength laser is shown in Fig. 3e. The lasing and spontaneous emission spectra for this laser at $T = 4$ K are shown in Supplementary Fig. S13. The physical volume of this laser is only $V \approx 0.2\lambda_o^3$, where λ_o is the lasing wavelength in air. Subwavelength lasers have been successfully implemented on other substrates by the use of plasmonics[29–31]. In our case, a purely semiconductor cavity mode alone provides enough confinement for subwavelength lasing without metal-optic effects[32,33]. Avoiding metal losses is a critical advantage that should allow high-efficiency laser operation.

Engineering these helical modes by controlling the nanopillar dimensions, we can select the mode number to be used for laser oscillation and control the wavelength of nanopillar laser emission. Because nanopillar cavities scale with growth time from the nanoscale throughout the microscale without critical dimensions, we can easily grow nanopillars to resonate at any wavelength of choice. Experimentally, we have verified that nanopillars support $n > 1$ resonances by directly imaging emission from nanopillars of different lengths, as presented in Fig. 3f–h with corresponding SEM images. For these measurements, we used nanopillars that were grown at oblique angles with respect to the surface normal of the substrate, allowing us to image emission along the nanopillar axes. Axial standing-wave patterns can be clearly discerned, confirming net propagation of nanopillar cavity modes along the nanopillar axis. As nanopillar length decreases, higher-order axial modes are cut off, such that fewer axial maxima can be observed. Nanopillars are held below threshold for these images to prevent speckle interference from obscuring the mode pattern. Traditional Fabry–Pérot modes cannot account for the patterns seen, because light leakage through the InGaAs–silicon interface is far too severe for such modes. Instead, we attribute the axial maxima to helically propagating modes of the nanopillar, which simulations have shown to be strongly supported despite even oblique junctions of low index contrast between nanopillars and substrate (see Supplementary Information).

We remark here that our experimental Q (~206) falls well short of theoretical estimates (for example, ~4,300 for TM_{61}), probably because tapering in the nanopillar perturbs the mode. To investigate the effects of the sidewall taper, additional FDTD simulations have been performed for nanopillars on silicon with 5° angles between opposite sidewalls. It should be noted that although 5° is a well-represented average, the range of taper angles can be from <3° to ~7°. Figure 4 shows vertical field profiles for TM_{61}, TM_{62} and TM_{63} modes, revealing the rather pronounced effects of tapering. The modes are noticeably confined towards the base of the nanopillar. At a certain height, the reduced nanopillar radius cuts off the mode in the vertical direction and reflects it downwards. The taper also blueshifts helical resonances (for example, ~37 nm blueshift for the TM_{61} mode), because the transverse dimensions become effectively smaller. Additionally, the adiabatic reduction of nanopillar radius causes helical modes to become less resonant as they propagate upwards, resulting in increased light leakage

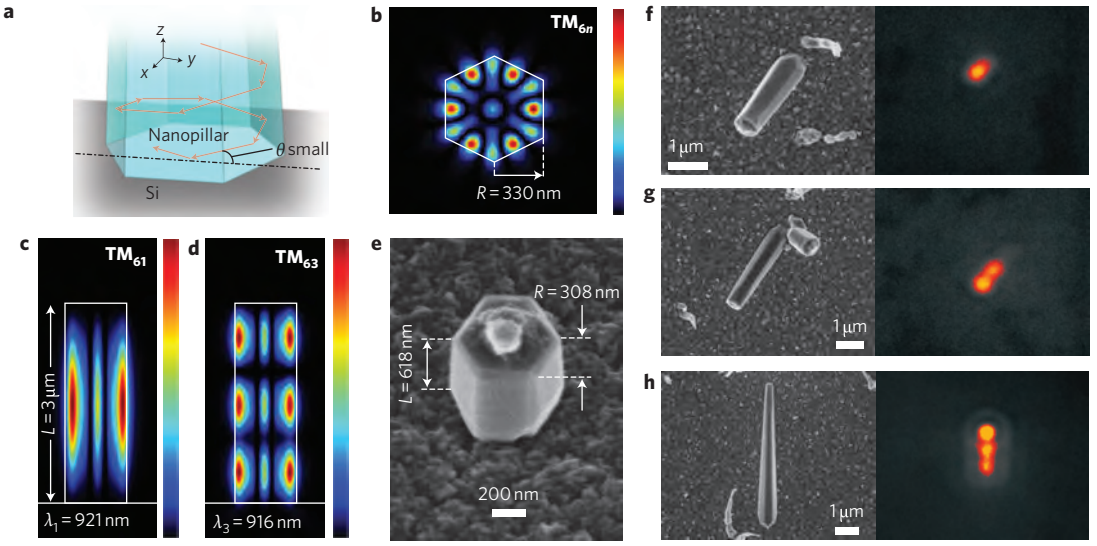

Figure 3 | Helically propagating modes for optical feedback of on-chip nanolasers. a, Schematic depicting how a helical ray path enables reflection from a low-index contrast interface due to glancing angle incidence, lending physical insight into the mechanism behind strong optical confinement in on-chip nanopillars. **b**, An FDTD-simulated field profile ($|E|^2$, linear scale) shows a hexagonal WG-like mode pattern (TM_{6n}) in the transverse plane, which arises from strong azimuthal components of helical modes. Such modes have net propagation along the nanopillar axis and build axial standing-wave patterns. **c**,**d**, First-order (**c**) and higher-order (**d**) standing waves. **e**, Strong light localization provided by helical modes enables nanolasers that are subwavelength on all sides. The SEM image shows such a subwavelength device. **f**–**h**, Experimental images of nanopillar emission show standing-wave patterns along the nanopillar axes, corroborating helical mode propagation. SEM images of the nanopillars are also shown.

through the cavity sidewalls. For TM_{61}, TM_{62} and TM_{63} modes, the Q factors are 319, 235 and 173, respectively. Although much smaller than the values of Q for straight nanopillars, these values agree extremely well with our experimental data, confirming that sidewall taper is the primary loss mechanism for our as-grown cavities. Engineering the taper angle thus offers an avenue to improve future laser performance. We briefly note that higher-order axial modes generally have lower quality factors. Physically, the stronger Fabry–Pérot characteristic of higher-order axial modes means that their effective longitudinal wave-vector components become stronger, causing larger penetration and loss into the substrate.

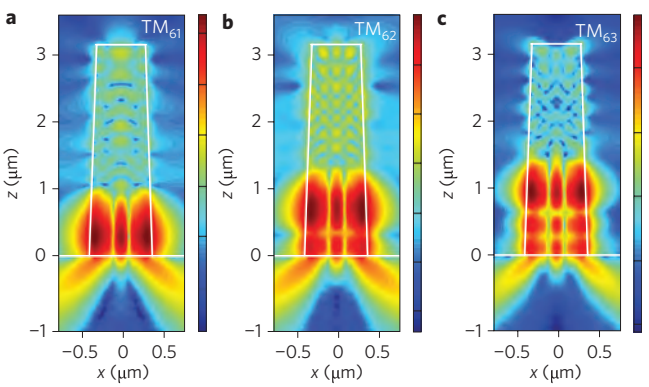

Figure 4 | Effects of nanopillar sidewall taper on optical modes. Vertical field profiles ($|E|^2$) are shown of a nanopillar on silicon with 5° taper for TM_{61}, TM_{62} and TM_{63} modes. The profiles here are plotted on a logarithmic scale (1 decade/tick) for clarity. The transverse field profiles are identical to that in Fig. 3b. Sidewall tapering results in increased light leakage, which decreases the quality factors of helical resonances to ~170–300. The smaller radius on the upper part of the pillar also introduces a mode cutoff such that helical modes are confined towards the base of tapered nanopillars. Tapering also blueshifts helical resonances.

Wavelength control of laser emission. By varying the indium composition of nanopillars during growth, we can spectrally match the semiconductor gain to designed cavity resonances to maximize spontaneous emission coupling into the cavity modes (see Supplementary Information)[34–36]. In this current study, we vary indium composition from 12 to 20% to achieve wavelength control of on-chip nanolasers over a ~50 nm range, as shown in Fig. 5. The flexibility of wavelength control may allow nanopillars to fulfill a myriad of laser applications throughout the near-infrared. For chip-scale silicon photonics applications, silicon-transparent laser light may be favourable to avoid absorption loss in silicon waveguides, although this is not required if transparent silica waveguides are used instead[37,38]. In the latter scenario, low-cost high-performance silicon photodetectors may then be used to complete the optical link. Nonetheless, we expect to be able to push nanopillar laser emission beyond silicon transparency, which would also improve cavity Q by removing absorption loss into the substrate. Past nanopillar growth studies have already demonstrated silicon-transparent nanopillar photoluminescence, indicating that a fundamental limitation does not exist for longer wavelength lasers[18]. The fact that we grow laser cavities using a bottom-up approach rather than top-down etching processes raises a couple of additional points of interest. First, single-crystal growth provides facets that are far smoother than etching can allow, thereby minimizing scattering loss. Additionally, the hexagonal structure of nanopillars is dictated by their hexagonal wurtzite crystal lattice. Thus, as-grown nanopillars have unprecedented symmetry, which prevents the polarization splitting of degenerate laser modes often seen in microdisks due to ellipticity. Instead, truly single-mode laser oscillation can be achieved.

Discussion

The scheme presented here for growing active nanophotonic components on silicon is promising for photonic integration with CMOS circuits. However, electrically pumped lasers are required for such applications. Although nanowire-based light-emitting diodes (LEDs) and lasers have been demonstrated, it remains

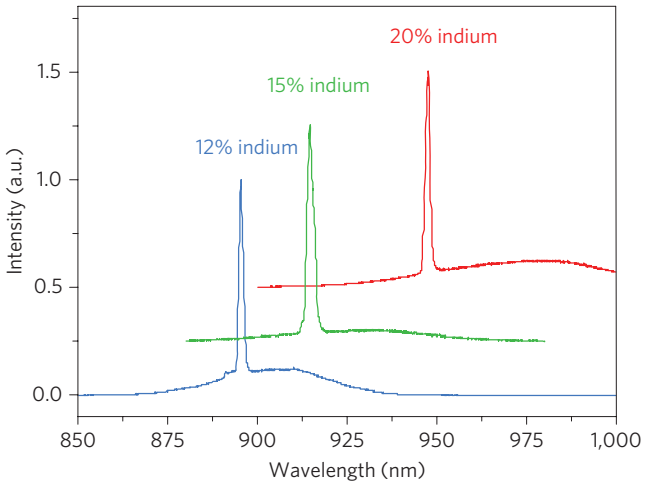

Figure 5 | Wavelength control of nanopillar lasers by composition variation. Nanopillar lasers can be implemented over a broad range of wavelengths by properly tuning indium composition and nanopillar dimensions. Nanopillars are grown to target dimensions designed to achieve resonances at specified wavelengths. Indium composition of the InGaAs core is concurrently adjusted so that nanopillar gain and emission spectrally match the resonant wavelength for laser oscillation. The spectra shown are offset for clarity. In this study, a change in indium composition from ~12–20% provides a 50 nm control in the output laser wavelength.

difficult to fabricate lasers and LEDs using as-grown nanostructures and conventional microfabrication techniques. The nanopillars discussed in this paper present significant advantages. Core–shell layering and doping capabilities greatly facilitate growth of p-i-n heterostructures and quantum wells in nanopillars[18]. Using such structures, electrical injection of as-grown nanopillar LEDs on silicon has already been achieved[20]. Notably, these devices were fabricated using standard contact lithography techniques because nanopillars are sizeable and robust. Future electrical contact schemes will account for preservation of nanopillar cavity modes to achieve electrically injected lasers on silicon.

Another critical aspect of silicon optoelectronics is coupling of laser emission into waveguides. From simulations of the helical cavity modes, we find that emission dominates in the in-plane radial direction (see Supplementary Information). Nanopillar lasers are thus compatible with the existing coupling schemes used for microdisks and ring resonators[11,39–41]. Additionally, various schemes have already been developed to turn in-plane light propagation into surface normal emission and vice versa[42–44]. Nanopillar lasers coupled to waveguides are thus promising for optical interconnects or any chip-scale device that requires an integrated light source.

Finally, note that modern CMOS electronics are fabricated on (100) silicon wafers. Although we presently use (111) silicon substrates to guarantee vertical alignment of nanopillars, this does not prevent nanopillar laser integration onto (100) silicon. (111) facets of a (100) silicon substrate can be exposed to grow nanopillars aligned at an angle of 54.7° with respect to the surface normal. We have shown that helical laser modes are still strongly supported, even for a larger 70° growth angle (see Supplementary Information).

In this Article, we demonstrate the first room-temperature III–V nanolaser grown on silicon with subwavelength volume. In doing so, we show that lattice mismatch is not a fundamental limit for monolithic integration of III–V photonic devices onto silicon, as is generally perceived. A bottom-up approach can provide an effective way of integrating nanophotonics with nanoelectronics. The ability to heavily populate an optically deficient silicon substrate with efficient III–V lasers has far-reaching implications for silicon photonics, particularly with regard to optical interconnects. With low-temperature nanopillar growth, the possibility exists for laser integration after electronics fabrication in CMOS foundries is complete. A new class of helically propagating modes implement our unique on-chip optical cavities, showing that optical phenomena in all-semiconductor nanostructures can be applied for practical on-chip nanophotonic devices. These modes may be taken advantage of for new designs of optical components such as photodetectors, modulators and solar cells. Meanwhile, future electrical operation of p-i-n nanopillar lasers on silicon promises for a powerful marriage between photonic and electronic circuits.

Methods

Nanopillar growth on silicon. To grow the InGaAs nanopillars, a silicon substrate was first cleaned with acetone, methanol and water (3 min for each step). The substrate was then deoxidized by buffered oxide etch for 3 min, and the surface mechanically roughened. Growth was subsequently carried out in an EMCORE D75 MOCVD reactor. Tertiarybutylarsine (TBA) was introduced to the reactor at temperatures higher than 200 °C. Before growth, *in situ* annealing at 600 °C was performed for 3 min. After annealing, the temperature was reduced to the growth temperature (400 °C in this work) in 3 min, followed by 2 min of temperature stabilization. Triethylgallium (TEGa) and trimethylindium (TMIn) were then introduced to the reactor to begin the 60 min InGaAs core growth. TMIn mole fractions were kept constant at 9.86×10^{-7}, 1.38×10^{-6} and 1.73×10^{-6} to achieve 12, 15 and 20% indium compositions, respectively. The TEGa mole fraction is held at 1.12×10^{-5}. All sources used a 12 l min^{-1} hydrogen carrier gas flow. The TBA mole fraction was 5.42×10^{-4}, giving a V/III ratio of ~43. A GaAs shell was then grown around the InGaAs core with the same TEGa and TBA mole fractions used for core growth, with a V/III ratio of 48. Room-temperature lasers use 90 nm shells with 20% indium cores, and low-temperature lasers typically have 30 nm shells and 15% indium cores. Nanopillar growth was vertically aligned to the (111) silicon substrate and was anisotropic with faster growth rates along the [0001] wurtzite c-axis. Nanopillar dimensions were linearly scalable with time, with no critical dimensions observed.

Lasing experiments. To achieve nanopillar laser oscillation, 120 fs pump pulses from a mode-locked Ti:sapphire laser (Coherent Mira, $\lambda_{pump} = 750$ nm, repetition rate 76 MHz) were delivered to the sample by a ×100, 0.7 numerical aperture (NA) objective (Mitutoyo NIR HR) at a temperature that was held between 4 K and 293 K by a continuous-flow liquid-helium cryostat (Oxford Instruments Hi-Res II). The pump spot size was slightly defocused to a diameter of ~6 μm. Nanopillar emission was collected by the same objective and relayed to a spectrometer and LN_2-cooled silicon charge-coupled device (Princeton Instruments SP2750 and Spec-10). Filters were used in all experiments to prevent pump light from reaching any detectors or cameras.

Received 26 September 2010; accepted 17 December 2010; published online 6 February 2011

References

1. Maiman, T. H. Stimulated optical radiation in ruby. *Nature* **187,** 493–494 (1960).
2. Miller, D. A. B. Device requirements for optical interconnects to silicon chips. *Proc. IEEE* **97,** 1166–1185 (2009).
3. Chen, G. *et al.* Predictions of CMOS compatible on-chip optical interconnect. *Integr. VLSI J.* **40,** 434–446 (2007).
4. Cloutier, S. G., Kossyrev, P. A. & Xu, J. Optical gain and stimulated emission in periodic nanopatterned crystalline silicon. *Nature Mater.* **4,** 887–891 (2005).
5. Pavesi, L., Dal Negro, L., Mazzoleni, C., Franzo, G. & Priolo, F. Optical gain in silicon nanocrystals. *Nature* **408,** 440–444 (2000).
6. Liu, J., Sun, X., Camacho-Aguilera, R., Kimerling, L. C. & Michel, J. Ge-on-Si laser operating at room temperature. *Opt. Lett.* **35,** 679–681 (2010).
7. Rong, H. *et al.* An all-silicon Raman laser. *Nature* **433,** 292–294 (2005).
8. Rong, H. *et al.* A continuous-wave Raman silicon laser. *Nature* **433,** 725–728 (2005).
9. Boyraz, O. & Jalali, B. Demonstration of a silicon Raman laser. *Opt. Express* **12,** 5269–5273 (2004).
10. Fang, A. W. *et al.* Electrically pumped hybrid AlGaInAs–silicon evanescent laser. *Opt. Express* **14,** 9203–9210 (2006).
11. Van Campenhout, J. *et al.* Electrically pumped InP-based microdisk lasers integrated with a nanophotonic silicon-on-insulator waveguide circuit. *Opt. Express* **15,** 6744–6749 (2007).
12. Lo, Y. H., Bhat, R., Hwang, D. M., Chua, C. & Lin, C.-H. Semiconductor lasers on Si substrates using the technology of bonding by atomic rearrangement. *Appl. Phys. Lett.* **62,** 1038–1040 (1993).
13. Chen, H. Z., Ghaffari, A., Wang, H., Morkoc, H. & Yariv, A. Low-threshold (~600 A/cm^2 at room temperature) GaAs/AlGaAs lasers on Si (100). *Appl. Phys. Lett.* **51,** 1320–1321 (1987).

14. Groenert, M. E. *et al.* Monolithic integration of room-temperature cw GaAs/AlGaAs lasers on Si substrates via relaxed graded GeSi buffer layers. *J. Appl. Phys.* **93,** 362–367 (2003).
15. Ujiie, Y. & Nishinaga, T. Epitaxial lateral overgrowth of GaAs on a Si Substrate. *Jpn J. Appl. Phys.* **28,** L337–L339 (1989).
16. Olsson, F., Xie, M., Lourdudoss, S., Prieto, I. & Postigo, P. A. Epitaxial lateral overgrowth of InP on Si from nano-openings: theoretical and experimental indication for defect filtering throughout the grown layer. *J. Appl. Phys.* **104,** 093112 (2008).
17. Moewe, M., Chuang, L. C., Crankshaw, S., Chase, C. & Chang-Hasnain, C. Atomically sharp catalyst-free wurtzite GaAs/AlGaAs nanoneedles grown on silicon. *Appl. Phys. Lett.* **93,** 023116 (2008).
18. Moewe, M., Chuang, L. C., Crankshaw, S., Ng, K. W. & Chang-Hasnain, C. Core–shell InGaAs/GaAs quantum well nanoneedles grown on silicon with silicon-transparent emission. *Opt. Express* **17,** 7831–7836 (2009).
19. Chen, R. *et al.* Second-harmonic generation from a single wurtzite GaAs nanoneedle. *Appl. Phys. Lett.* **96,** 051110 (2010).
20. Chuang, L. C. *et al.* InGaAs QW nanopillar light emitting diodes monolithically grown on a Si substrate. *Conference on Lasers and Electro-Optics*, CMFF6 (OSA, 2010).
21. Chuang, S. L. *Physics of Optoelectronic Devices* 337–393 (Wiley, 1995).
22. Coldren, L. A. & Corzine, S. W. *Diode Lasers and Photonic Integrated Circuits* 185–261 (Wiley, 1995).
23. Baba, T. Photonic crystals and microdisk cavities based on GaInAsP-InP system. *IEEE J. Sel. Top. Quant. Electron.* **3,** 808–830 (1997).
24. Bjork, G. & Yamamoto, Y. Analysis of semiconductor microcavity lasers using rate equations. *IEEE J. Quant. Electron.* **27,** 2386–2396 (1991).
25. McCall, S. L., Levi, A. F. J., Slusher, R. E., Pearton, S. J. & Logan, R. A. Whispering-gallery mode microdisk lasers. *Appl. Phys. Lett.* **60,** 289–291 (1992).
26. Nobis, T. & Grundmann, M. Low-order optical whispering-gallery modes in hexagonal nanocavities. *Phys. Rev. A* **72,** 063806 (2005).
27. Wiersig, J. Hexagonal dielectric resonators and microcrystal lasers. *Phys. Rev. A* **67,** 023807 (2003).
28. Chen, R., Chuang, L. C., Tran, T., Moewe, M. & Chang-Hasnain, C. Spatially resolved, polarized photoluminescence from wurtzite InGaAs/GaAs nanoneedles. *Conference on Lasers and Electro-Optics*, JWA95 (OSA, 2010).
29. Hill, M. T. *et al.* Lasing in metallic-coated nanocavities. *Nature Photon.* **1,** 589–594 (2007).
30. Oulton, R. F. *et al.* Plasmon lasers at deep subwavelength scale. *Nature* **461,** 629–632 (2009).
31. Hill, M. T. *et al.* Lasing in metal-insulator-metal sub-wavelength plasmonic waveguides. *Opt. Express* **17,** 11107–11112 (2009).
32. Nezhad, M. P. *et al.* Room-temperature subwavelength metallo-dielectric lasers. *Nature Photon.* **4,** 395–399 (2010).
33. Yu, K., Lakhani, A. & Wu, M. C. Subwavelength metal–optic semiconductor nanopatch lasers. *Opt. Express* **18,** 8790–8799 (2010).
34. Kuykendall, T., Ulrich, P., Aloni, S. & Yang, P. Complete composition tunability of InGaN nanowires using a combinatorial approach. *Nature Mater.* **6,** 951–956 (2007).
35. Qian, F. *et al.* Multi-quantum-well nanowire heterostructures for wavelength-controlled lasers. *Nature Mater.* **7,** 701–706 (2008).
36. Pan, A. *et al.* Continuous alloy-composition spatial grading and superbroad wavelength-tunable nanowire lasers on a single chip. *Nano Lett.* **9,** 784–788 (2009).
37. Kawachi, M. Silica waveguides on silicon and their application to integrated-optic components. *Opt. Quant. Electron.* **22,** 391–416 (1990).
38. Suzuki, S., Shuto, K. & Hibino, Y. Integrated-optic ring resonators with two stacked layers of silica waveguide on Si. *IEEE Photon. Tech. Lett.* **4,** 1256–1258 (1992).
39. Bogaerts, W. *et al.* Nanophotonic waveguides in silicon-on-insulator fabricated with CMOS technology. *J. Lightwave Technol.* **23,** 401–412 (2005).
40. Ando, S., Kobayashi, N. & Ando, H. Hexagonal-facet laser with optical waveguides grown by selective area metalorganic chemical vapor deposition. *Jpn J. Appl. Phys.* **34,** L4–L6 (1995).
41. Choi, S. J., Djordjev, K., Choi, S. J. & Dapkus, P. D. Microdisk lasers vertically coupled to output waveguides. *IEEE Photon. Tech. Lett.* **15,** 1330–1332 (2003).
42. Taillaert, D. *et al.* An out-of-plane grating coupler for efficient butt-coupling between compact planar waveguides and single-mode fibers. *IEEE J. Quant. Electron.* **38,** 949–955 (2002).
43. Mahler, L. *et al.* Vertically emitting microdisk lasers. *Nature Photon.* **3,** 46–49 (2009).
44. Koseki, S., Zhang, B., De Greve, K. & Yamamoto, Y. Monolithic integration of quantum dot containing microdisk microcavities coupled to air-suspended waveguides. *Appl. Phys. Lett.* **94,** 051110 (2009).

Acknowledgements

This work was supported by the Defense Advanced Research Projects Agency (DARPA) University Photonics Research (UPR) Award HR0011-04-1-0040, Microelectronics Advanced Research Corp (MARCO) Interconnect Focus Center (IFC) and the Department of Defense (DoD) National Security Science and Engineering Faculty Fellowship. C.C.H. acknowledges support from the Chang Jiang Scholar Endowed Chair Professorship at Tsinghua University, China, and the Li Ka Shing Foundation Women in Science Research Grants. R.C. acknowledges support from a National Defense Science and Engineering Graduate Fellowship. The authors thank Cun-Zheng Ning and E.K. Lau for fruitful discussions.

Author contributions

C.C.H. proposed and guided the overall project. R.C., T.-T.D.T, K.W.N. and C.C.H. designed the experiments. R.C. and T.-T.D.T. performed optical measurements. K.W.N., W.S.K. and L.C.C. developed and performed material growth. K.W.N. and W.S.K. performed SEM measurements. R.C., T.-T.D.T. and F.G.S. studied and simulated the optical mode. R.C. performed gain modelling and rate equation analysis. R.C. and C.C.H. composed the manuscript.

Additional information

The authors declare no competing financial interests. Supplementary information accompanies this paper at www.nature.com/naturephotonics. Reprints and permission information is available online at http://npg.nature.com/reprintsandpermissions/. Correspondence and requests for materials should be addressed to C.C.H.